Tuning Molecular Relaxation for Vertical Orientation in Cylindrical Block Copolymer Films via Sharp Dynamic Zone Annealing

6 AUTHORS, INCLUDING:

D.-M. Smilgies
Cornell University
262 PUBLICATIONS **5,531** CITATIONS

SEE PROFILE

Manish Kulkarni
Indian Institute of Technology Kanpur
34 PUBLICATIONS **555** CITATIONS

SEE PROFILE

David G. Bucknall
Heriot-Watt University
158 PUBLICATIONS **2,396** CITATIONS

SEE PROFILE

Alamgir Karim
University of Akron
307 PUBLICATIONS **6,945** CITATIONS

SEE PROFILE

Tuning Molecular Relaxation for Vertical Orientation in Cylindrical Block Copolymer Films via Sharp Dynamic Zone Annealing

Gurpreet Singh,[†] Kevin G. Yager,[‡] Detlef-M. Smilgies,[§] Manish M. Kulkarni,[†] David G. Bucknall,[||] and Alamgir Karim*,[†]

[†]Department of Polymer Engineering, The University of Akron, Akron, Ohio 44325, United States
[‡]Center for Functional Nanomaterials, Brookhaven National Laboratory, Upton, New York 11973, United States
[§]Cornell High Energy Synchrotron Source (CHESS), Cornell University, Ithaca, New York 14853, United States
[||]School of Materials Science and Engineering, Georgia Institute of Technology, Atlanta, Georgia 30332, United States

S *Supporting Information*

ABSTRACT: Fabricating vertically ordered and etchable high aspect ratio nanodomains of block copolymer (BCP) thin films on diverse substrates via continuous processing dynamic cold zone annealing (CZA) is particularly attractive for nanomanufacturing of next-generation electronics. Previously, we reported dynamic CZA studies with a shallow thermal gradient (maximum $\nabla T \sim 14$ °C/mm) that produced only BCP cylinders oriented parallel to substrate. Here, we report a CZA utilizing a dynamic sharp thermal gradient ($\nabla T \sim 45$ °C/mm) (i.e., CZA-S). This method allows for production of

CZA-S Velocity (V)

etchable and vertically oriented cylindrical domains of poly(styrene-*b*-methyl methacrylate) in 100−1000 nm thick films on low thermal conductivity rigid (quartz) and flexible (PDMS, Kapton) substrates. Competing substrate wetting interactions dominate BCP orientation in films below 100 nm while broadening of the thermal gradient profile in films thicker than 1000 nm leads to loss of vertical orientation. An optimal dynamic sweep rate (~5 μm/s) produces the best vertical order. At too fast a sweep rate (>10 μm/s) the BCP film ordering is kinetically hindered, while at too slow a sweep rate (<1 μm/s), polymer relaxation and preferential surface wetting dynamics favor parallel BCP orientation. Equivalent static gradient conditions produce vertically aligned BCP cylinders only at the maximum ∇T. CZA-S mechanism involves propagating this vertically oriented BCP zone across the sample.
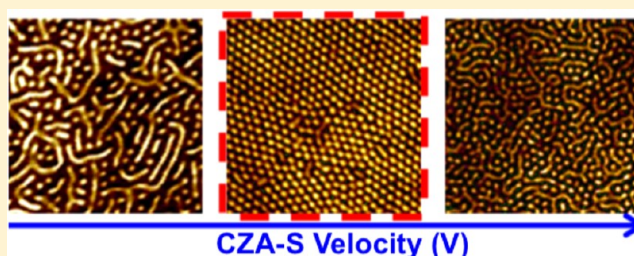
INTRODUCTION

Block copolymers undergo spontaneous phase separation at the nanoscale, forming a diversity of self-assembled structures with functional architectures, such as lamellae, cylinders, and gyroids. Block copolymer (BCP) produce nanostructures that have periodicity in the range of 5−100 nm,[1] making them a highly attractive alternative route to nanopatterning compared to the present limit using photolithography is 22 nm half-pitch via 193 nm light.[2] Several researchers[3−9] have demonstrated that it is indeed possible to obtain nanopatterns based on highly ordered BCPs, but translating these to manufacturable large area patterns with minimal or no defects is a major challenge requiring facile directed assembly methods that can be adopted by industry. Such methods will open avenues for exciting areas of application of BCPs in, for example, organic photovoltaic devices (OPVs) where it is expected that the very high interfacial area of the blocks with $\sim$10−20 nm domain spacing would be useful for exciton separation[10,11] or serve as templates for directed assembly of nanoparticles that may even have interesting implications for plasmonics and opto-electronics as has been demonstrated by several researchers.[12−15] More recently, pioneering studies have explored BCP nanostructures

for nanoporous membrane formation for ultrafiltration concepts,[16−19] which would benefit from directed alignment of channels in vertical orientations favoring fluid transport.

Various methods have been developed for directed assembly of BCP phase orientation including shear alignment,[20] electric field alignment,[21] solvent annealing,[22] thermal techniques including temperature gradients,[23−28] zone casting,[29] topographic[30] and chemical[31] patterning, gradient substrate surface energy,[32] and even nanoscale roughness.[33] Of these, few methods are applicable to the continuous production of the desired BCP morphology over large areas needed for most nanotechnological applications, a primary reason for the disconnect between lab-scale experiments and scale up to intermediate and large-scale device manufacturing processes. Thus, the practical reality of achieving these ordered BCP structures with scalable continuous processing methods on flexible substrates as needed for nanomanufacturing still remains a formidable challenge. Here we demonstrate the

viability of applying a dynamic gradient thermal annealing process to vertically ordering BCPs. This process is inherently extendible to established roll-to-roll (R2R) technology, providing a facile route toward continuous large-area fabrication of highly ordered nanomaterials. Moreover, the use of flexible substrates makes this processing method immediately applicable to target applications in flexible organic electronics and photovoltaics.

Zone annealing is a well-established method predominantly utilized in metallurgical and semiconductor purification processes, where recrystallization and oriented grain growth occur on a planar front formed by the cooling edge of the annealed zone.[25] In contrast to "hot" zone annealing of BCPs[23,24] where the maximum temperature (T_{max}) of the thermal zone is above the order−disorder transition temperature (T_{ODT}), causing the two blocks to intermix completely; we perform zone annealing in the "cold" regime where $T_{max} < T_{ODT}$, but above the glass transition temperature (T_g) of either of the blocks. Hence, this process is known as cold zone annealing (CZA). We previously[26] applied this process to create highly ordered BCP cylinders that are parallel to the substrate with desirable features of orientational control, long-range order, and faster ordering kinetics than conventional oven annealing. Although directed thermal zones have been utilized for ordering organic systems, including BCPs[23−26,28] and organic electronics,[34,35] its potential to vertically order BCPs has not been investigated to date despite its simplicity and viability as an industrially adaptable method. This paper reports how a modification of the existing CZA method, previously demonstrated to produce well-ordered parallel cylinders, produces vertically ordered BCP microstructures in thin films important to nanotechnology applications.

In the present study, the heating section of the previously developed CZA equipment was modified by narrowing the ~1 cm wide heated zone into a ~1 mm narrow hot zone using a hot wire heater. This modification, in conjunction with utilization of substrates with a thermal conductivity at least 100 times lower than silicon, produces a 3-fold sharper thermal gradient field ($\nabla T_{max} \sim 45$ °C mm^{-1}), in contrast to our previous studies ($\nabla T_{max} \sim 15$ °C mm^{-1}), and we consequently refer to this approach as CZA-Sharp (CZA-S). We demonstrate that the use of sharp thermal gradients enables the formation of vertically oriented cylinders of PS−PMMA BCP films (100−1000) nm thick, while simultaneously improving the in-plane order of hexagonally packed domains.

■ EXPERIMENTAL SECTION

BCP Materials. Thin film samples of poly(styrene-*block*-methyl methacrylate) (PS−PMMA) diblock copolymer were used in these studies. The total molar mass along with the polydispersity and mass fraction of PMMA, indicated in parentheses, respectively was 47.5 kg mol^{-1} (1.07, 0.26) and 82 kg mol^{-1} (1.07, 0.3), bought from Polymer Source Inc. and used as obtained. The mass fraction of PMMA leads to formation of hexagonally packed cylinders upon microphase separation with cylinder to cylinder spacing $L_0 \approx 24$ and 50 nm for 47.5 and 82 kg mol^{-1}, respectively. The material safety data sheet provided by Polymer Source Inc. indicates that the glass transition temperature (T_g) for the PS block is 107 °C and for the PMMA block is 126 °C for the 47.5 kg mol^{-1} PS−PMMA system whereas for the 82 kg mol^{-1} PS−PMMA system T_g is 110 °C for PS block and 124 °C for PMMA block. The order−disorder transition temperature (T_{ODT}) for high molecular mass PS-*b*-PMMA, including the BCP used in this study, is not accessible, i.e., $T_{ODT} \gg T_g$. Deuterated PS−PMMA "dPS−PMMA" diblock copolymer was used in these studies for R-SANS

measurements. The PS block was deuterated; total molar mass of the diblock copolymer and mass fraction of PMMA respectively were 77 kg mol^{-1} and 0.26. Diblock copolymer had 1% low molecular weight PMMA impurity. Deuterated diblock copolymer was provided by Center for Nanophase Materials Sciences, Oak Ridge National Laboratory, and used as obtained.

Substrate Preparation. Amorphous quartz substrates and p-type silicon substrates were bought from Chemglass, Inc., and Silicon Quest International, Inc., respectively. Amorphous quartz and silicon substrates were rinsed in toluene followed by 1 h of ultraviolet-ozone (UVO) treatment. 50 μm thick polyimide films "DuPont Kapton PV 9101" (Kapton) were provided by DuPont and used as obtained. Sylgard-184, a two-part thermocurable polydimethyloxysilane (PDMS) elastomer (Dow Corning Corp.), was employed for making PDMS substrates. A mixture of PDMS elastomer and curing agent in 10:1 weight ratio was poured on glass microscope slides and deaerated in vacuum. Curing was done at 120 °C for 6 h PDMS was then peeled off the glass slide to obtain 1.5−2 mm thick substrates. PDMS substrates thus obtained are hydrophobic in nature with surface energy of 18−20 mJ m^{-2} as measured by contact angle analysis. UVO exposure oxidizes the surface and makes the substrate hydrophilic, and it was observed that long time (greater than 8 h) UVO exposure of PDMS substrates increases the surface energy to ~68 mJ m^{-2}.

BCP Film Deposition. BCP films of thickness (h) were spin-coated from toluene solution onto cleaned substrates, as described above. Film thicknesses were determined using a thin film interferometer, (F-20 UV Thin Film Analyzer, Filmetrics, Inc.) with a resolution of 1 nm. Spin-coating conditions were adjusted so as to get predetermined thicknesses in the range $0.5L_0 \leq h \leq 32L_0$. Prior to the annealing process, residual solvent was extracted by drying samples at 60 °C for 24 h under vacuum. Oven-annealed samples were kept in a vacuum oven at 210 °C for 24 h to achieve a morphology that did not evolve further with time. The temperature gradient (∇T) was varied from 5 to 45 °C mm^{-1} depending on substrate used. ∇T_{max} values of 45 and 15 °C mm^{-1} were obtained for films coated on quartz substrates (thermal conductivity[36] of 1.4 W m^{-1} K^{-1}), whereas for achieving a gradient of 5 °C mm^{-1}, films were coated on silicon substrates (thermal conductivity[36] of 148 W m^{-1} K^{-1}). Samples that were cold zone annealed experienced a dynamic ∇T_{max} (45, 15, or 5 °C mm^{-1}) with maximum temperature "T_{max}" of 210 °C at sample translation rates from 0.1 to 15 μm s^{-1} depending on the experiment.

Cold Zone Annealing. The basic structural design of our modified zone annealing apparatus is based on the design concept described previously by Lovinger et al.[37] The cold blocks are cooled by circulating low molecular weight PDMS oil ("Thermal C10" Julabo USA Inc.) at −5 °C using a chiller system (Julabo F12-ED refrigerated/heating circulator). The hot zone is generated by a low resistance (0.025 Ω cm^{-1}) nickel−chrome wire covered with a 3 mm (outer diameter) ceramic insulation that is powered with a high current source (Digital DC Power Supply, Model 1692, B&K Precision Corp.). For the present experiments the cold blocks are separated from the nickel−chromium wire at a distance of 1 mm. The height of nickel−chrome wire is fine-tuned so as to achieve desired ∇T_{max} on the substrate. The temperature gradients thus produced are characterized using a thermal IR imaging camera having an accuracy of 0.1 °C (Testo 875 Thermal Imager Kit).

Thin Film Characterization. Topography of these films was imaged using a Dimension Icon atomic force microscope (AFM) (Bruker AXS) in the Peak Force Quantitative Nanomechanical Property mapping mode, followed by digitization of the images (using "ImageJ (NIH)") for quantitative statistical analysis. Grazing-incidence small-angle x-ray scattering (GISAXS) measurements were performed at the D1 beamline of the Cornell High Energy Synchrotron Source (CHESS) and at the X9 beamline of the National Synchrotron Light Source (NSLS) at Brookhaven National Laboratory. At CHESS D1, 9.8 keV X-ray photons with a 1.5% bandwidth from a multilayer monochromator impinged on thin film samples coated on silicon wafers at an angle of 0.12°, at the first waveguide resonance of the film. GISAXS images were collected with a CCD camera (MedOptics) at 1493 mm from the sample. The CCD was

protected from the intense scattering in the incident plane with a rodlike beamstop. Sample alignment and measurement of the reflectivity curve close to the film critical angle was performed with an ion chamber. At the NSLS X9, an incident X-ray beam of energy 13.5 keV (wavelength = 0.0918 nm) was used. Samples were measured under vacuum (~40 Pa). GISAXS experiments were performed over a range of incidence angles, both below and above the film−vacuum critical angle, with data collected using a charged-coupled device (CCD) detector. Data conversion to q-space was accomplished using silver behenate powder as a standard. Rotational small-angle neutron scattering (R-SANS) data were obtained on the LOQ small-angle diffractometer at the ISIS Pulsed Neutron Source (STFC Rutherford Appleton Laboratory, Didcot, U.K.). This is a "white beam" time-of-flight instrument that utilizes neutrons with wavelengths, λ, between 0.2 and 1 nm. Data are simultaneously recorded on two, two-dimensional, position-sensitive, neutron detectors to provide a simultaneous Q range of 0.08−16 nm^{-1}. Each sample and background was placed in the beam and was measured for a sufficient amount of time in order to gather data of high statistical precision. Each raw scattering data set was then corrected for the detector efficiencies, sample transmission, and background scattering and converted to scattering cross-section data ($\partial\Sigma/\partial\Omega$ vs Q) using the instrument-specific software (Colette). These data were placed on an absolute scale (cm^{-1}) using the scattering from a standard sample (a solid blend of hydrogenous and perdeuterated polystyrene).

Image Analysis. AFM images were digitized using image analysis software called ImageJ (NIH). AFM images were first converted to 8-bit gray scale images followed by performing "thresholding" function. Processed images were then analyzed for particle size area fraction. Area fractions of parallel and perpendicular cylinders were thus calculated. Images of these calculations are given in Supporting Information Figure S1.

UVO Etching. PS−PMMA films were exposed to UVO environment inside a Novascan PSD Series UV Ozone System for specific time periods. Measured ablation rate is ~1.33 nm min^{-1}. After desired exposure time, films were rinsed with heptane and dried in nitrogen. These films were then exposed to UV light in absence of oxygen for 15 min and then washed with glacial acetic acid and distilled water in succession.

■ RESULTS AND DISCUSSION

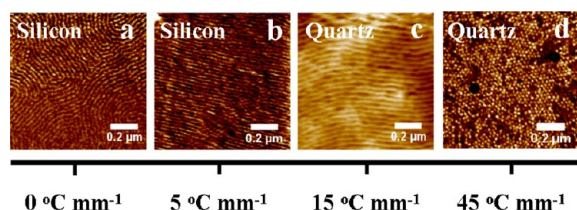**Transition from Parallel to Vertical Orientation of PS−PMMA from CZA to CZA-S.** Figure 1 illustrates the AFM

Figure 1. AFM images (a−d) of CZA annealed thin films (150 nm thick) of PS−PMMA (47.5 kg mol^{-1}) at varying ∇T_{max}: (a) 0 °C mm^{-1} (silicon substrate), (b) 5 °C mm^{-1} (silicon substrate), (c) 15 °C mm^{-1} (quartz substrate), and (d) 45 °C mm^{-1} (quartz substrate).

topographical patterns for 150 nm thick PS−PMMA (total number-average molecular weight, M_n = 47.5 kg mol^{-1}) films subjected to a wide range of ∇T_{max} (0−45 °C mm^{-1}). The reference sample (Figure 1a) was heated uniformly, i.e., ∇T_{max} = 0 °C mm^{-1}, inside a vacuum oven for 24 h. By comparison for samples annealed by CZA, i.e., ∇T_{max} > 0, a T_{max} of 210 °C was used with a sample translation velocity of 1 μm s^{-1}. It is worth noting that T_{ODT} for 47.5 kg mol^{-1} PS−PMMA is inaccessible (~410 °C, when $\chi N \approx 10.5$).[38] Figures 1a and 1b correspond to samples coated on silicon substrates, and Figures

1c and 1d correspond to samples coated on quartz substrates (see Experimental Section for film preparation procedure). Contact angle analysis reveals that surface energy of UVO treated silicon and quartz were found to be comparable, i.e., 71 and 69 mJ m^{-2}, respectively. Therefore, Figures 1a−1d can be directly compared on the basis of $|\nabla T_{max}|$. Figures 1b and 1c, wherein the PS−PMMA thin film experiences a relatively shallow ∇T_{max} (5 and 15 °C mm^{-1}), show long-range well-ordered cylinders laying parallel to the substrate. These results are in agreement with those obtained by Yager et al.[25] and Berry et al.[26] However, when an identical sample was subjected to a ∇T_{max} = 45 °C mm^{-1}, well-packed vertically oriented cylinders were obtained.

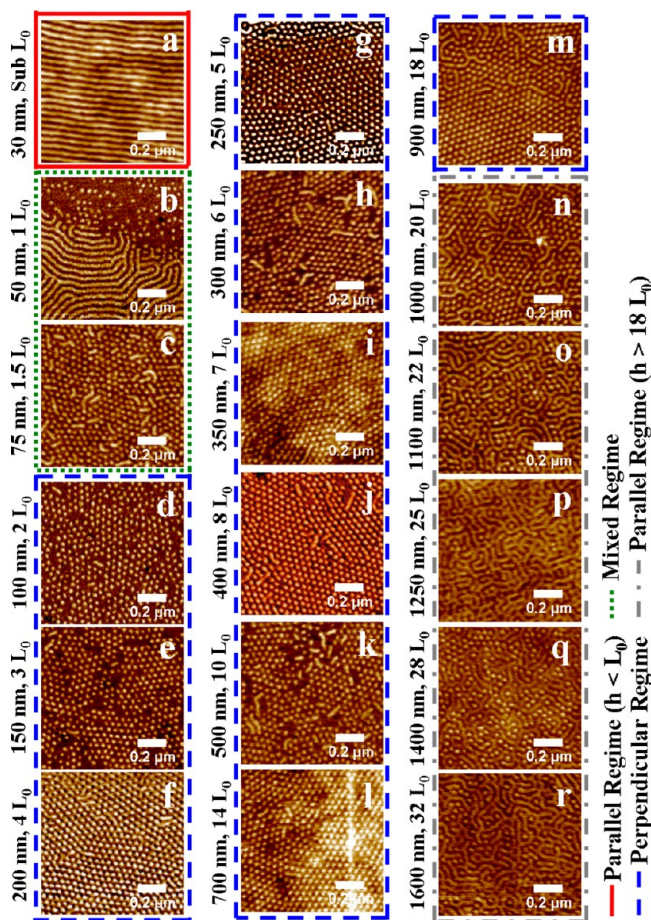**Summary of Orientation Thickness Regimes of PS−PMMA on Quartz via CZA-S.** Figure 2 shows a compendium

Figure 2. AFM images of CZA-S annealed (210 °C T_{max}, 1 μm s^{-1}, and 45 °C mm^{-1}) PS−PMMA (82 kg mol^{-1}) thin films on quartz substrate with varying film thickness: (a) 30, (b) 50, (c) 75, (d) 100, (e) 150, (f) 200, (g) 250, (h) 300, (i) 350, (j) 400, (k) 500, (l) 700, (m) 900, (n) 1000, (o) 1100, (p) 1250, (q) 1400, and (r) 1600 nm. Note: cylinder-to-cylinder spacing (L_0) ≈ 50 nm; layer-to-layer spacing ≈ 45 nm.

of CZA-S annealed PS−PMMA (M_n = 82 kg mol^{-1}) thin films from h = 30 nm or sub L_0 to h = 1600 nm or 32 L_0 (where h is film thickness and cylinder-to-cylinder spacing, L_0 ≈ 50 nm) exposed to a gradient ∇T_{max} of 45 °C mm^{-1} and translational velocity of 1 μm s^{-1}. There is a strong dependence of CZA-S annealed PS−PMMA cylinder orientation on film thickness. Using image analysis software (procedure explained in
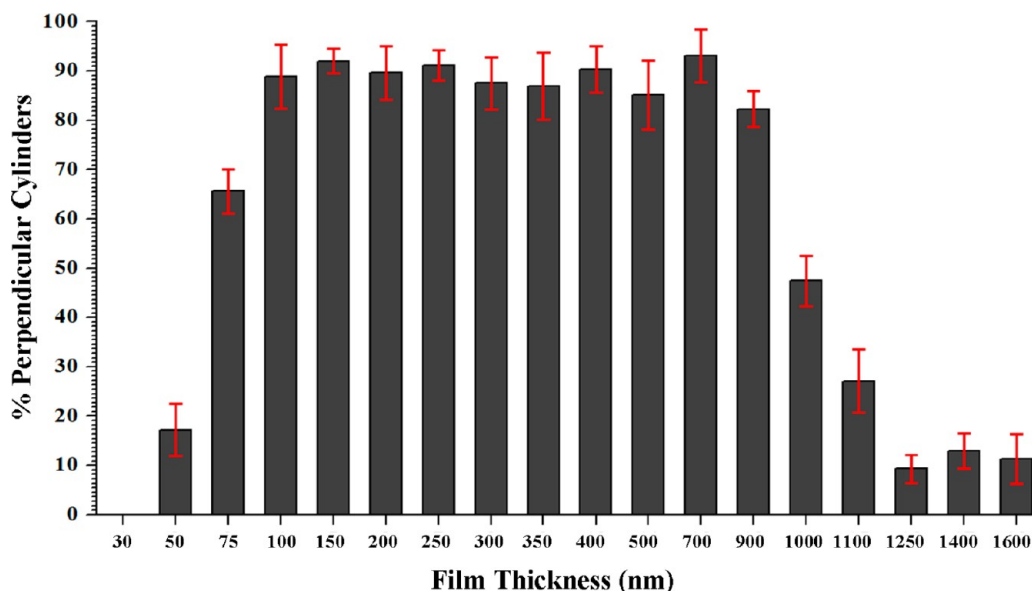
Figure 3. Histogram of changing cylinder composition with PS−PMMA (82 kg mol^{-1}) film thickness. Note: cylinder-to-cylinder spacing (L_0) ≈ 50 nm; layer-to-layer spacing ≈ 45 nm.

Experimental Section) the relative cylinder percentage is determined (Figure 3), which is defined as the ratio of perpendicular oriented areas, excluding regions with no surface morphology.

On quartz substrates, four thickness regimes of ordering are identified: (i) sub-L_0 thicknesses, which produced well-ordered cylinders laying parallel to the substrate; (ii) thicknesses greater than or equal to L_0 and less than $2L_0$, which produced a mixed morphology; (iii) thicknesses greater than or equal to $2L_0$ and less than or equal to $18L_0$, which produced predominantly hexagonally packed cylinders oriented perpendicular to the substrate; and (iv) thicknesses greater than $18L_0$, which produced a mixed oriented morphologies. For this BCP L_0 = 50 nm, so the thickness range measured spans from submonolayer to ∼37 parallel cylinder layers. From a technological and scientific viewpoint, the film thickness regime of $2L_0$ to $18L_0$ where cylinders orient perpendicular when utilizing CZA-S is of most interest. Therefore, we will discuss this regime in detail below. Regimes i, ii, and iv are discussed in detail in the Supporting Information.

Vertical Orientation Regime in Thin to Thick PS−PMMA Films on Quartz. The result of the CZA-S process is to orient the PMMA domains of the BCP in a fashion that is different to what is observed using conventional oven thermal annealing; evidently, the in-plane thermal gradient induces reorientation of the microphase. A detailed mechanism of the orientation process for CZA-S of PS−PMMA films is described in a subsequent section in the paper. Internal morphology and lateral ordering of CZA-S annealed BCP films were investigated in real space (Figure 4a), via AFM of sequentially ablated top surface of PS−PMMA films, as well as in inverse space via grazing-incidence small-angle X-ray scattering (GISAXS) (Figure 4b) and rotational small-angle neutron scattering (R-SANS) (Figure 4c).

CZA-S annealed PS−PMMA films were exposed to UVO environment for controlled time periods that causes degradation of both the domains. Controlled UVO exposure followed by rinsing with a nonsolvent (to avoid surface reconstruction, use of a nonsolvent is essential), such as heptane and distilled

water, ablates a predetermined portion of the top layer depending on the time of UVO exposure, which makes it possible to measure the internal film morphology via AFM. (After each UVO/nonsolvent treatment, the PMMA domain at the top layer of the film was selectively etched to enhance contrast between the PS and PMMA domains.) This procedure has been adopted from a recent paper by Albert et al.[39] They prove this procedure to be in agreement with film cross-section results via transmission electron microscopy (TEM). Figure 4a shows the change in film morphology of a 250 nm thick PS−PMMA film from the top to the bottom of the film at different height intervals. Topography of the 250 nm thick film is composed of predominantly well-packed perpendicular cylinders. 100 nm from the top, the predominantly perpendicular morphology still dominates. Approximately 150 nm from the top, a mixed morphology appears. This is the tipping point where the perpendicular cylinders seen at the top are replaced by the parallel cylinders that are aligned with respect to the substrate. Perpendicular cylinders almost completely disappear ∼200 nm from the top. Real-space analysis reveals that a CZA-S annealed PS−PMMA thin film has a dual morphology of well-packed perpendicular cylinders near the top surface of the film and substrate-aligned parallel cylinders near the substrate. We observe that thicker films, in this regime of ordering, reveal an identical structure, i.e., the base layer approximately 100−150 nm thick of parallel cylinders followed by vertical cylinders. Nealey et al.[40,41] have made similar observations for PS−PMMA films up to 600 nm thick on a neutral surface that were annealed at a neutral annealing temperature (230 °C).

GISAXS reveals bimodal film morphology, as shown in Figure 4b. The incident angle was chosen to be at the first waveguide resonance, just above the critical angle of the film. This way the film as a whole was homogeneously illuminated while the scattering was dynamically enhanced. The X-ray beam was incident perpendicular to the zone annealing direction. The 2D GISAXS image shows scattering features both in the parallel and the perpendicular direction. The vertical streaks are associated with perpendicular cylinder morphology in the surface-near region, as observed with AFM. Note that only the
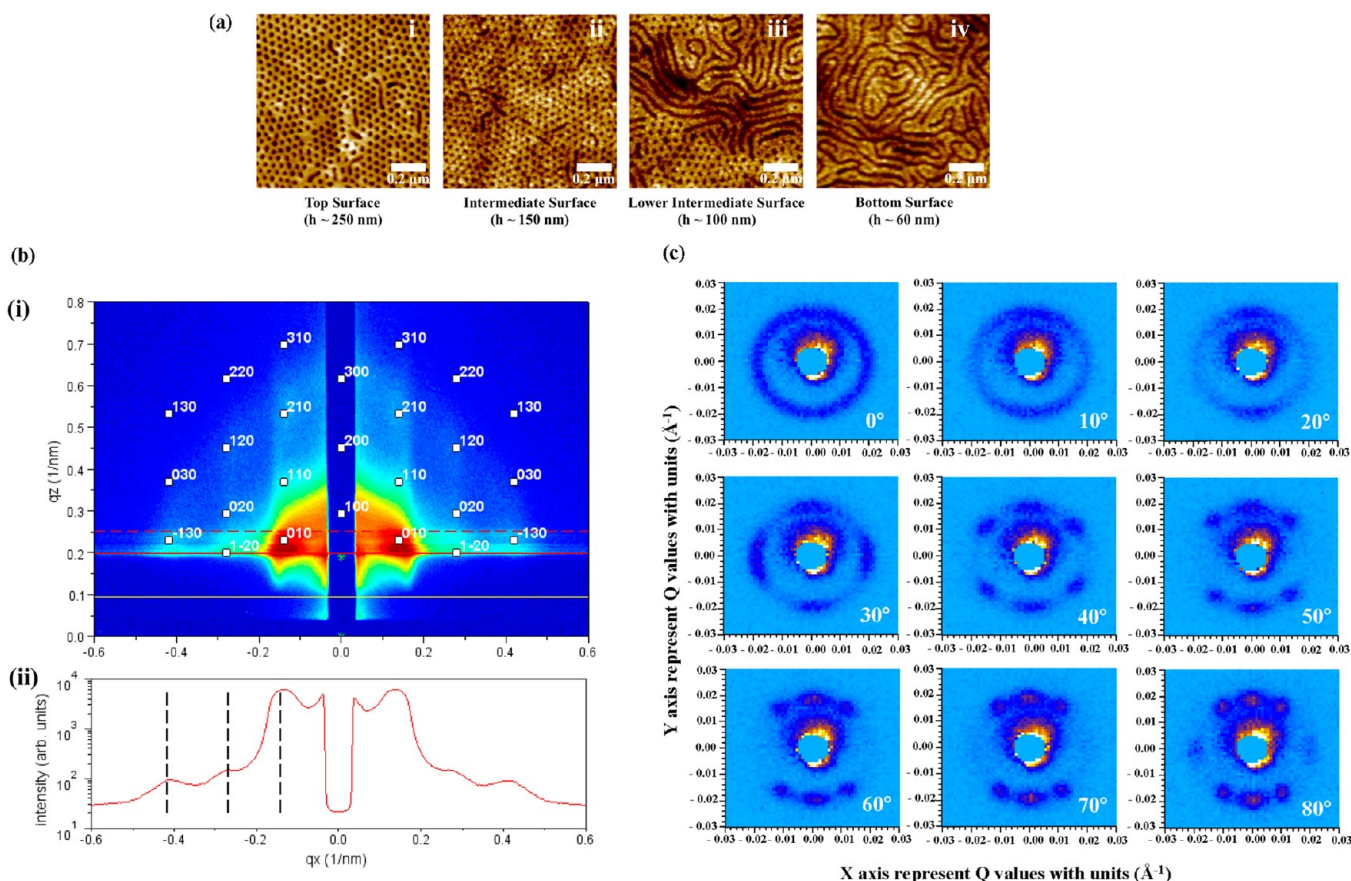
Figure 4. (a) AFM images of 250 nm thick CZA-S annealed (210 °C T_{max}, 1 μm s^{-1}, and 45 °C mm^{-1}) PS−PMMA (82 kg mol^{-1}) films that were sequentially ablated from the top surface: (i) morphology at top surface; (ii) morphology 100 nm into the film; (iii) morphology 150 nm into the film; (iv) film morphology 190 nm into the film. (b) (i) GISAXS image of a CZA-S annealed 200 nm thick PS-*b*-PMMA film. The yellow line indicates the sample horizon; the red solid and dashed lines indicate the film and the substrate critical angles, respectively, defining the Yoneda band of enhanced scattering. The 2D image shows both weak vertical streaks and broad spots. The spots could be indexed to a hexagonal cylinder lattice with a lattice constant of 45 nm corresponding to lying cylinders at the film−substrate interface. The streaks were associated with standing cylinders close to the film surface. (ii) Integrated intensity of the above image in the Yoneda band. Weak streaks show only at integer multiples of the first-order peak. The X-ray beam perpendicular to the annealing direction. This is consistent with the AFM observation of a laterally oriented cylinder lattice. (c) Rotational small-angle neutron scattering (R-SANS) data of a CZA-S annealed 250 nm *d*PS−PMMA film on quartz substrate. Scattering data were collected at angles ranging from 0° (i.e., normal to the substrate) to 80° at an increment of 10° per measurement.

$\sqrt{1}$ and $\sqrt{4}$ order streaks are observed, not the $\sqrt{3}$ order streak. In conjunction with the X-ray beam impinging perpendicular to the zone annealing direction, this finding supports the AFM local results that the film was laterally oriented. Apart from the clearly observed streaks, the GISAXS image also shows broad diffraction spots that can be indexed to a hexagonal lattice with a lattice constant of ~45 nm. The width of the broad spots indicates that the domain sizes of the parallel or perpendicular oriented BCPs are reasonably small. These data are typical for cylinders lying parallel to the substrate with the first layer forming close-packed parallel cylinders on the substrate surface. It is well-known that the polar PMMA block has a much higher affinity toward the native silicon oxide layer than the PS block. Hence, we expect cylinders to lie parallel to the film−substrate interface. The horizontal positions of the vertical streaks due to the surface-near standing cylinders and the horizontal positions of the spots due to the lying cylinders at the interface coincide. The block copolymer formed a consistent microphase-separated structure, albeit with different orientation at the two interfaces. Detailed *in situ* and *ex situ* GISAXS measurements are planned in future experiments in

order to elucidate the CZA-S mechanism and film morphology quantitatively.

R-SANS measurements, shown in Figure 4c, of deuterated PS−PMMA BCP films (refer to the Experimental Section for material information) at angles ranging from 0° (i.e., normal to the substrate) to 80° at an increment of 10° per measurement confirm the presence of the bimodal orientation of the PMMA cylinders both perpendicular and parallel to the substrate. Qualitatively, R-SANS reveals that vertically oriented cylinders are approximately equal in amount to parallel cylinders. What is interesting about this bimodal system is that both vertical and parallel cylinders are oriented with respect to the substrate with a very small isotropic distribution. This is corroborated by R-SANS data that show an absence of isotropic structure in the scattering patterns.

CZA-S-Induced PS−PMMA Orientation on Flexible Substrates. The CZA process is only as effective as the dynamic ∇T_{max} that can be generated. Naturally thermal conductivity of the substrate thus plays a significant role, with lower thermal conductivity materials (quartz, mica, sapphire, etc.) preserving a sharp thermal gradient, whereas conductive substrates (copper, silicon, etc.) tend to broaden it substan-

tially. Future flexible electronics applications will require processing methods applicable to flexible substrates. There is a natural match between the CZA processing method and flexible substrates, which generally have low thermal conductivities, and are ideally suited to roll-to-roll methods. There have been very few studies so far that have tackled the challenges of ordering BCP thin films on flexible substrates. Russell and co-workers[42] demonstrated that it is indeed possible to generate very well-ordered arrays of block copolymer nanostructures on flexible substrates. It is worthy to note that those flexible substrates were prepatterned so as to assist the process of block copolymer self-assembly. Here we demonstrate that CZA-S can effectively fabricate high-aspect-ratio well-packed vertically oriented PS−PMMA cylinders directly onto flexible substrates via a continuous roll-to-roll process with an added advantage that the substrate need not be prepatterned.

Thermal conductivities of Kapton and PDMS are 0.37 and 0.15 W m^{-1} K^{-1}, respectively.[43] Kapton is stable well above 210 °C, and therefore T_{max} in the CZA-S process was kept at 210 °C and the optimal ∇T_{max} was found to be ∼45 °C mm^{-1}. Contact angle analysis of the Kapton substrate revealed that it has an inherent surface energy of 42 mJ m^{-2}, which is very close to surface energies of both PS and PMMA. Therefore, Kapton can potentially behave as a neutral substrate[32] for PS−PMMA thin films. Owing to the lower thermal stability of PDMS, T_{max} for CZA processing for this substrate was restricted to 175 °C. From an engineering point of view, even though T_{max} was 175 °C, owing to the lower thermal conductivity of PDMS than quartz, it was still possible to attain a ∇T_{max} of 45 °C mm^{-1}. Figure 5 shows that the PS−PMMA morphologies obtained on PDMS and Kapton are identical to the morphologies obtained on quartz substrates for identical thickness regimes, and these results are explained in detail in the Supporting Information. Recently, it has been reported[40] that oven annealing of cylindrical PS−PMMA at temperatures at and above 210 °C yields perpendicular cylinders since it is believed that at such high temperatures the air−polymer interface behaves as a neutral surface energy layer for block copolymer ordering. However, the fact that well-packed perpendicular cylinders were accessible even at a T_{max} of 175 °C for 250 nm (Figure 5c) and 700 nm (Figure 5d) thick films indicates that mechanism of PS−PMMA ordering via CZA-S process is not a consequence of the high-temperature neutral surface energy layer concept; instead, it rather seems to be related to the dynamic ∇T_{max} of the CZA-S process.

Mechanism of CZA-S-Induced BCP Ordering. The most intriguing aspect of the CZA-S process is the mechanism by which a sharp dynamic ∇T induces vertical orientation through the majority of the film thicknesses. The kinetic response of a substrate-confined polymeric thin film to temperature can be broadly classified into two time scales: instantaneous asymmetric normal expansion followed by slower isotropic relaxation over several hours. Beaucage et al.[44] reported that the isotropic relaxation is coupled with anisotropic flow-induced shear in response to the thermal expansion. Isothermal temperature-jump measurements[44] on substrate confined thin films reveals that the observed viscosity is larger in the plane of the film than in the normal direction. Beaucage et al.[44] explained this phenomenon as due to preferential chain orientation normal to the film caused by rapid normal expansion and if given sufficient time these films relax toward equilibrium, i.e., a fully isotropic state. They conclude that films
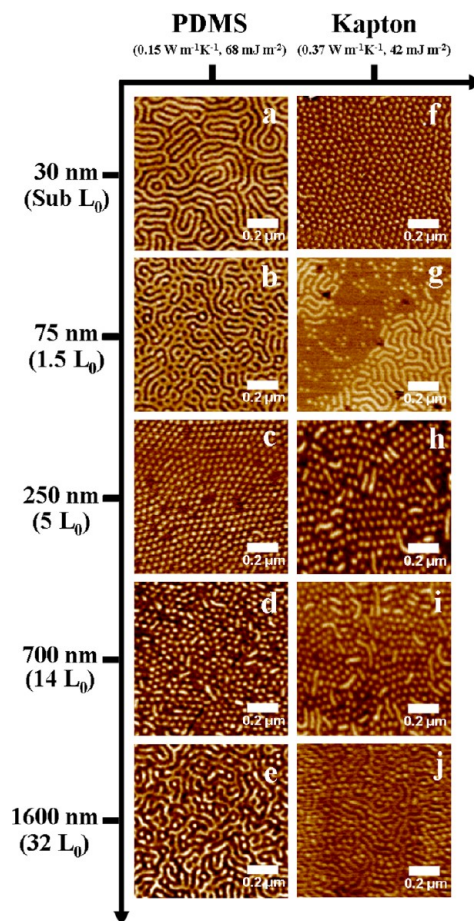

Figure 5. AFM images of CZA-annealed PS−PMMA (82 kg mol^{-1}) thin films on PDMS (a−e) and Kapton (f−j) substrates with varying thickness: (a, f) 30, (b, g) 75, (c, h) 250, (d, i) 700, and (e, j) 1600 nm. Substrate thermal conductivity (W m^{-1} K^{-1}) and surface energy (mJ m^{-2}) are indicated. Note: layer-to-layer spacing ≈45 nm.

quenched below their T_g's at short times exhibit a metastable state of preferred chain orientation relative to the thermal expansion. The thermal response of polymer chains in the limit of short and long time scales is highly relevant to the dynamic ∇T CZA-S process as discussed below.

The CZA-S process induces a gradient in the normal expansion of the film that is swept across the entire sample, whereas a uniform temperature generates a homogeneously normal expansion across the whole sample. Additionally, unlike in case of uniform annealing where entire film relaxes at the same time, in a dynamic ∇T field only a fixed zone relaxes at a particular time, and this zone is swept through the entire film. The temperature gradient profile of the CZA-S process can be divided into two regions: "sharp" and "broad" as shown in Figure 6a. The characteristic exposure time of the sample exposed to sharp or broad regions are "Δt_{sharp}" and "Δt_{broad}", respectively, and depend on sample velocity. For brevity, we simply refer to these characteristic times as t_{sharp} and t_{broad}. Table 1 shows the annealing exposure times, T_{sharp} and T_{broad}, as a function of sample velocity, which are estimated as the time taken for the sample to be heated from T_g up to maximum set temperature and cool back down to T_g in the CZA-S annealing zone. In order to quantitatively help explain the phenomena of vertical orientation of PS−PMMA films via the CZA-S process, we compare the CZA-S exposure time to the relaxation time
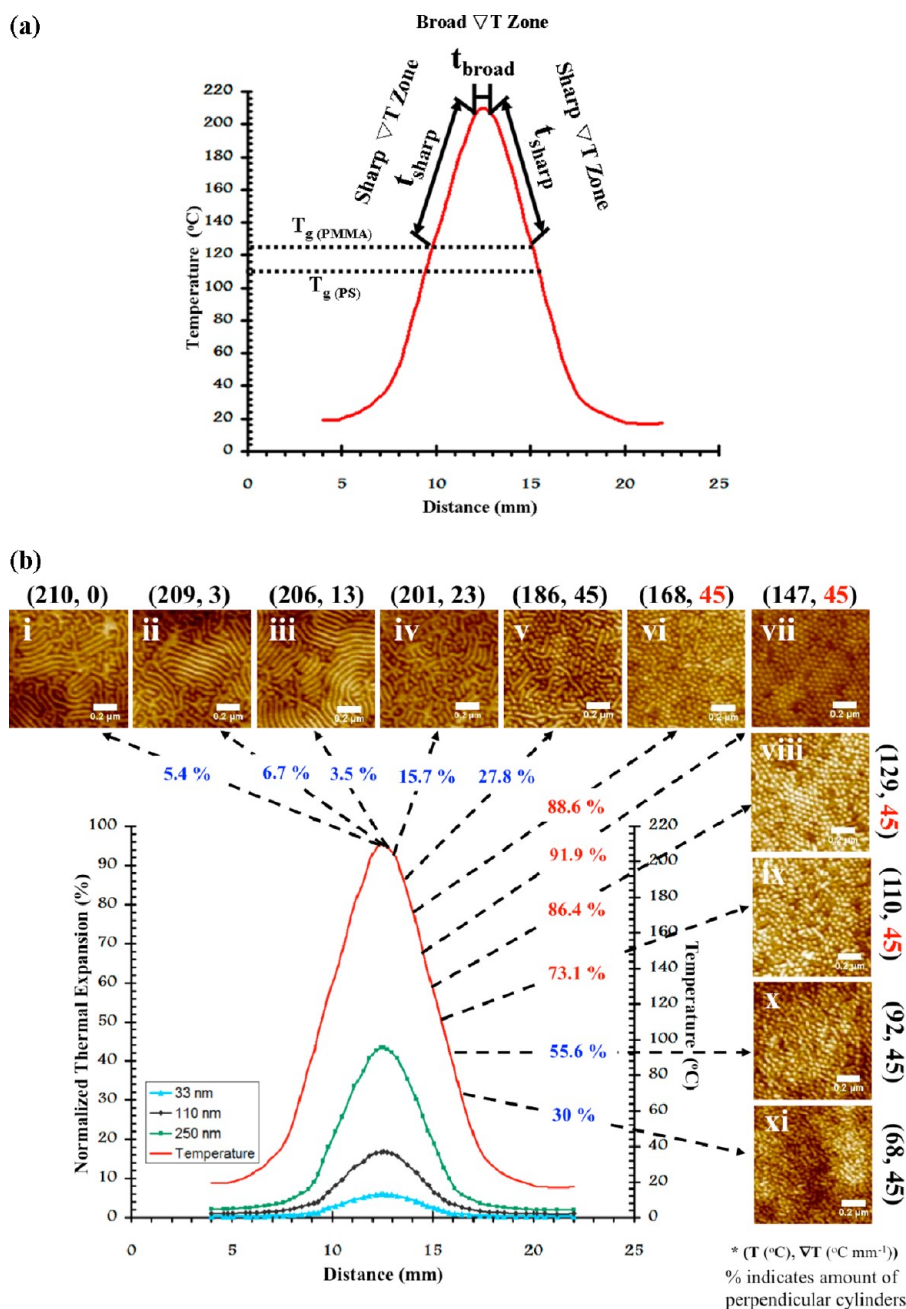
(a)

(b)

Figure 6. (a) Plot of temperature gradient profile produced via CZA-S process on quartz substrate. t_{sharp} and t_{broad} are the exposure times that a sample experiences for the demarked zones in a CZA-S process. (b) Plot showing gradient normal expansion of PS−PMMA thin films normalized to the cylinder-to-cylinder spacing ($L_0 \sim 50$ nm) generated in presence of a sharp ∇T_{max} of 45 °C mm^{-1}. AFM images of static CZA-S experiments on PS−PMMA (82 kg mol^{-1}) are shown as well.

Table 1. Variation of Exposure Times, in Sharp and Broad Regions of Gradient Temperature Profile, with Sample Translation Rate and Relaxation Times "τ" for Sharp "τ_{sharp}" and Broad "τ_{broad}" Regions[a]

velocity (μm s^{-1})	$T_{sharp} = 2t_{sharp}$ (min)	$T_{broad} = t_{broad}$ (min)
0.1	833 ($>\tau_{sharp}$)	167 ($>\tau_{broad}$)
0.5	167 ($>\tau_{sharp}$)	33 ($>\tau_{broad}$)
1	83 ($>\tau_{sharp}$)	17 ($\approx\tau_{broad}$)
5	17 ($<\tau_{sharp}$)	3 ($\ll\tau_{broad}$)
15	6 ($\ll\tau_{sharp}$)	1 ($\ll\tau_{broad}$)

[a]$\tau_{broad} = \tau_{Tmax} = \tau_{210\,°C} \approx 20$ min. $\tau_{sharp} = \tau_{upper\,quartile} = \tau_{175\,°C} \approx 37$ min.

(τ) as calculated by Beaucage et al.[44] As a first order of approximation, it is assumed that the relaxation behavior of PS−PMMA thin films is the same as PMMA thin films and estimate their relaxation times via a reference 130 kg mol^{-1} PMMA at various temperatures as observed by Beaucage et al. The relaxation time for a temperature above 180 °C was obtained by extrapolation of Beaucage's[44] experimental data. We compare T_{sharp} and T_{broad} with τ_{sharp} and τ_{broad}, respectively, where τ_{sharp} and τ_{broad} are representative relaxation times for sharp and broad ∇T regions and estimated at 175 °C (approximately the upper quartile temperature in the sharp region) and at 210 °C (T_{max} of CZA-S), respectively. Note we could equally have selected a different lower temperature of
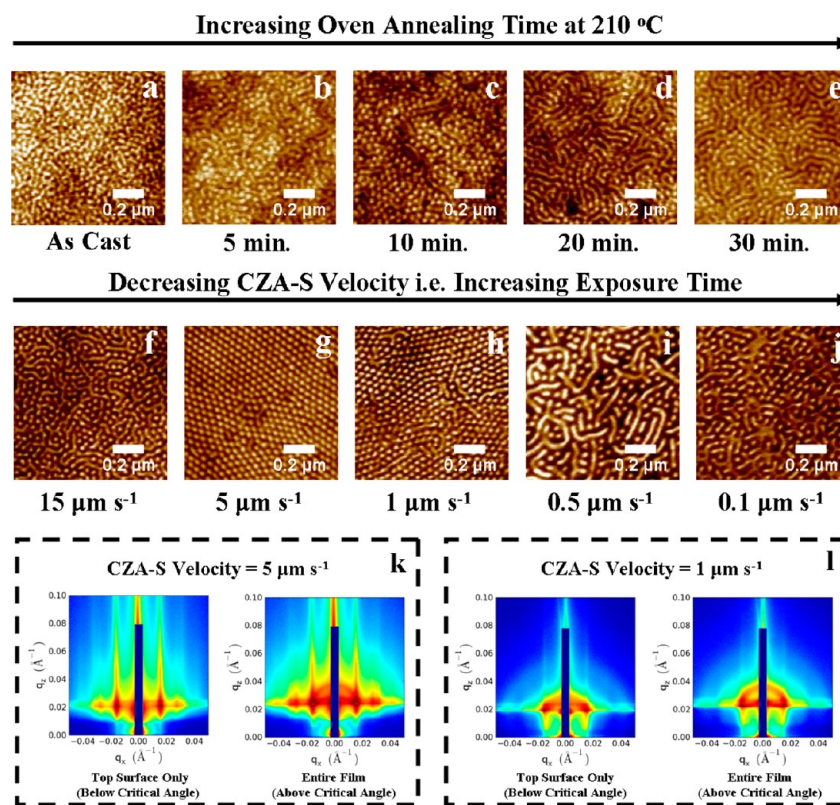
Figure 7. AFM images (a−e) of oven-annealed PS−PMMA (82 kg mol^{-1}) film at time intervals of 0, 5, 10, 20, and 30 min, respectively. AFM images (f−j) of CZA-S-annealed PS−PMMA thin film that were annealed with sample translation velocities of 15, 5, 1, 0.5, and 0.1 μm s^{-1}, respectively. GISAXS images of CZA-S annealed PS−PMMA films, with incident X-ray angle below and above polymer critical angle, at sample translation velocities of 5 and 1 μm s^{-1} are shown in (k) and (l), respectively. GISAXS images (k) and (l) correspond to morphology shown in (g) and (h), respectively. Samples were etched at identical conditions to enhance scattering contrast.

τ_{sharp} and τ_{broad} while maintaining the same differential temperature. We will now carry this mechanism of CZA-S discussion forward by breaking up into relevant components: (A) effects of the static ∇T, (B) comparative oven annealing, and (C) dynamic ∇T sweep rate.

Effect of Static Temperature Gradient (∇T). *Potential Expanded Film Thickness Commensurability Effect.* Block copolymer films are known to have properties that depend on the film thickness commensurability. As discussed before, the gradient temperature profile causes a gradient normal film expansion profile. Figure 6b shows the calculated thermal expansion profiles for polymer films experiencing the CZA process with a ∇T_{max} of 45 °C mm^{-1}, using raw data from the literature[45] and assuming that the coefficient of thermal expansion for both PS and PMMA are very similar. These data show that the thin film normal expansion increases with increasing film thickness and is estimated to be ∼10% of the local unannealed film thickness after in-plane confinement is accounted for. Yager et al.[46] observed oscillations in block copolymer orientation due to commensurability effects on a steep film thickness gradient (∼4000 nm/mm) on nanoparticle decorated surface. Likewise, Zhang et al.[47] recently published a paper where they observed commensurability oscillations in morphology due to steep thickness gradients (∼2000 nm/mm) as well. The thermal expansion gradient from CZA-S process is however much shallower ∼10 nm/mm, so that across the 2.5 mm wide CZA-S gradient zone the expansion would be 25 nm or 0.5 domain thickness (L_0), relative to the film thickness, h that spans $2L_0$ (∼100 nm) to $20L_0$ (∼1000 nm). A variation of

$0.5L_0$ may have been expected to induce an incommensurate thickness for the film thickness $h \sim 2L_0$; however, this is not observed. Thus, we conclude that, in CZA-S, incommensurate thickness arising from as-cast incommensurate film thickness and/or from thermal film expansion gradient does not play a dominant role in underlying mechanism of vertical orientation of PS−PMMA cylinders observed in CZA-S.

Potential Film Gradient Confinement Effect. We performed CZA-S under *static (nonmoving)* conditions to decouple the spatial effects of ∇T from the dynamic motion effects of CZA-S. Static CZA-S was undertaken by holding the sample stationary for 6 h on the CZA-S setup (Figure S2, Supporting Information). It is important to note that the annealing time of 6 h is equivalent to the reptation time of 130 kg mol^{-1} PMMA at 132 °C. This implies that the entire film shown in Figure 6b had sufficient time to relax to its equilibrium morphology. Figure 6b shows the diversity of structures at different ∇T's after 6 h of static annealing. The temperature gradient curve is symmetric about T_{max}, and each sample position on the temperature gradient curve experiences a fixed temperature and temperature gradient. The AFM images show that parallel cylinders are formed at the zone experiencing a T_{max} of 210 °C with the lowest ∇T of 0 °C mm^{-1}, consistent with results obtained for uniform oven annealing at 200 and 210 °C. Figures 6b (i to iv) shows that the perpendicular component of cylinders increases as temperature decreases modestly from 210 to 201 °C; however, ∇T increases significantly from 0 to 23 °C mm^{-1}. Figure 6b (v to viii) shows that perpendicular orientation is maximized as the ∇T reaches a maximum of 45

°C mm^{-1} at a temperature of 147 °C. Further decrease of temperature to 130 °C while maintaining a ∇T of 45 °C mm^{-1} produces additional reduction of the degree of BCP perpendicular orientation. The perpendicular morphology is specific to the region with ∇T_{max} of 45 °C mm^{-1}.

The above measurements lead us to propose that a gradient strain induced by normal thermal expansion under lateral confinement leads to perpendicular morphology. Such a strain field varies directly with ∇T (strain field is maximum when ∇T is maximum (∇T_{max}) and minimum when ∇T is minimum (∇T_{min})), and even though the block copolymer had enough time for relaxation in the region of ∇T_{max}, the gradient strain field maintains the perpendicular morphology that has developed. Physically, for a sharp ∇T, a narrow zone of polymer melt undergoing thermal expansion will be surrounded by rigid glassy polymer, and this will lead to a gradient lateral strain-confinement effect, which favors vertically oriented block copolymer to maximize the packing density in the system, i.e., minimize stress from horizontally oriented cylinders near polymer melt-glassy region. This is analogous to BCP orientation on sinusoidal patterned substrates as reported by Pickett et al.[48] They observed vertically oriented BCP microdomains, which they attributed to frustration effects near the pattern boundary. They reasoned that frustration leads to high stress areas, which makes parallel orientation of BCP microdomains unfavorable. Similarly, absence of frustration effects in the region with shallow ∇T favors horizontal cylinder orientation. This is in accordance to observations in Figure 6b (i to iii).

From a practical point of view, the ∇T_{max} region is a very narrow zone of ~2.5 mm; therefore, static CZA-S is not a viable method to attain desired perpendicular morphology over large areas. Dynamic CZA-S annealing offers a practical solution by moving the zone with ∇T of 45 °C mm^{-1} and propagating vertical order throughout the sample. The vertical orientation of CZA-S annealed thin films with ∇T of 45 °C mm^{-1} showed excellent correspondence with static annealing results. This suggests that the mechanism of the dynamic process is to propagate the narrow (2.5 mm) perpendicular orientation zone morphology throughout the film.

Potential Film Surface Tension Gradient Effect. A gradient temperature profile gives rise to a gradient surface tension field along the surface of the film. Taking polystyrene as a reference, simple calculations reveal that its surface tension varies from 40.7 to 27.4 mN m^{-1} as temperature varies from 20 to 210 °C, respectively, and more significantly a surface tension gradient of ~7 mN m^{-1} is generated in the narrow zone of sharp ∇T from 120 to 200 °C. This in-plane surface tension gradient field must stretch the block copolymer chains in-plane that favors their parallel orientation at the surface and within the film. However, as will be seen in the section on CZA-S sweep rates, in-plane surface tension field influences horizontal BCP morphology only at slow annealing rates or high annealing times, i.e., when annealing time is much greater than total relaxation time of the film.

Uniform Thermal Oven Annealing. PS−PMMA films were annealed in a vacuum oven at 210 °C (Figure 7a−e) to compare with temporal effects observed in CZA-S processing (Figure 7f−j). The immediate interesting observation is that, quantitatively (refer Table 2), both sets undergo nonmonotonic ordering, with a maximum in vertical ordering at intermediate annealing/exposure times. Table 2 gives the changing perpendicular cylinder fraction with annealing speed and

Table 2. Variation Perpendicular Cylinder Fraction with Changing Oven Annealing Time and Changing CZA-S Annealing Rate

sample description (corresponding Figure)	% perpendicular cylinders
5 min oven-annealed (Figure 7b)	44
10 min oven-annealed (Figure 7c)	65
20 min oven-annealed (Figure 7d)	10
30 min oven-annealed (Figure 7e)	9
CZA-S 15 μm s^{-1} (Figure 7f)	43
CZA-S 5 μm s^{-1} (Figure 7g)	97
CZA-S 1 μm s^{-1} (Figure 7h)	84
CZA-S 0.5 μm s^{-1} (Figure 7i)	12
CZA-S 0.1 μm s^{-1} (Figure 7j)	7

time. Interestingly, recall a similar nonmonotic vertical ordering behavior was observed spatially (not temporally as is the case here) in static gradient (Figure 6b (i to xi)) along the temperature gradient. The combined static temperature gradient and uniform oven annealing provide a measure of the nonmoving spatiotemporal component of dynamic (moving) CZA.

We discuss uniform oven annealing in more detail now. When the exposure time is less than 5 min, we observe the as-cast poorly ordered cylindrical morphology, and as time increases to 10 min, we observe considerable (65%) vertical population of PMMA cylinders, although they are not hexagonally packed. As the exposure time becomes greater than or equal to 20 min, we observe that morphology has developed into predominantly (10%) cylinders laying parallel to the surface. Therefore, we conclude that there exists an optimum annealing time to obtain the desired morphology (vertical, parallel, mixed), minimally at the surface if not in the bulk, even with conventional thermal oven annealing. To our knowledge, this short annealing time transient ordering phase has not been reported before for thermally annealed films. An analogous phenomenon of optimum annealing time does exist for solvent-annealed cylindrical BCP films.[49,50] Tsarkova et al. reported a transitory morphology for solvent-annealed BCP films that form relief structures. They observed the transition from perpendicular cylinders to parallel cylinders along with advent of relief structures when the BCP thin films (<100 nm) were solvent-annealed for increasing time periods. Again, this is quite different to our observations because of three major reasons: (1) thermal annealing and solvent annealing are completely different processes, (2) solvent annealing is not effective for films thicker than 100 nm, and (3) we do not observe relief structures for films in regime iii. Evidently, an instantaneous and spatially asymmetric thermal expansion of the polymer film above its glass transition temperature T_g induces a vertical strain field that orients polymer chains into perpendicular cylinders (Figure 7b,c), albeit random with lots of defects. Under uniform heating, this transient expansion induced ordering is followed by isotropic chain relaxation at relatively longer times (20 min), leading to an increase in parallel cylinder population (Figure 7d,e) driven by preferential surface wetting of lower surface energy PS block. We note that τ at 210 °C is ~20 min, consistent with an equilibrium morphology of predominantly parallel cylinders when sample exposure time or annealing time is greater than or equal to 20 min.

Effect of CZA-S Sweep Rates. An optimal CZA-S sweep rate exists for vertical ordering since in-plane surface tension,

surface wetting effects, and polymer relaxation at longer time intervals compete with the CZA-S process to induce parallel orientation. Figure 7f−j shows the morphology of PS−PMMA thin films that were CZA-S annealed at different sweep rates. Table 2 shows the changing perpendicular cylinder fraction with CZA-S annealing rate. Surface wetting effects and relaxation effects are dominant at low CZA-S dynamic rates (0−1 μm/s) (Figure 7h−j, with % perpendicular cylinders decreasing from 84% to 7%, respectively), leading to an observed optimal dynamic rate of CZA-S annealing of (1−5) μm/s for maximal (97%) vertical oriented morphology (Figure 7g). Table 1 shows how the sample exposure time varied with sample translation velocity. Exposure time for the broad ∇T region in Figure 7i,j exceeds τ_{broad} (refer Table 1 for quantitative values), so that the perpendicular morphology obtained in the region of sharp ∇T_{max} is subsequently lost as the polymer has enough time to relax and attain the equilibrium surface wetting morphology in passing across the broad ∇T. Once the block copolymer attains its stable equilibrium morphology in the broad region, it cannot revert back to the perpendicular morphology as it passes through the cooling region again. Figure 7g,h shows hexagonally packed perpendicular morphology; however, it can be clearly seen that the perpendicular morphology developed in Figure 7g has fewer defects (97% perpendicular cylinders) than that developed in Figure 7h (84% perpendicular cylinders). We can understand these differences and the high degree of vertical ordering for both figures better by considering the associated T_{sharp} and T_{broad} relative to τ_{sharp} and τ_{broad}. As listed in Table 1, relaxation times are $\tau_{sharp} \approx 37$ min and $\tau_{broad} \approx 20$ min. Figure 7g corresponds to a sample translation (sweep) rate of 5 μm s^{-1} for which $T_{sharp} = 17$ min and $T_{broad} = 3$ min. Likewise, Figure 7h corresponds to a sample sweep rate of 1 μm s^{-1} for which $T_{sharp} = 83$ min and $T_{broad} = 17$. For both sweep rates T_{broad} is less than τ_{broad} so that the polymer did not have sufficient time to relax in the broad ∇T region, leading to a high degree of vertical ordering for both samples. In Figure 7h, T_{sharp} for sample translation rate of 1 μm s^{-1} is greater than τ_{sharp} while T_{broad} is nearly approaching τ_{broad}. Consequently, Figure 7h has more defects (parallel orientation) than Figure 7g. Figure 7f shows morphology developed for a sample translation rate of 15 μm s^{-1} for which T_{sharp} and T_{broad} are 6 and 1 min, respectively, times that are clearly insufficient for ordering to occur so that the morphological development is in its nascent stage. Therefore, there exists an upper and lower critical sweep rate that leads to a poor vertical ordering morphology. When the translation rates are too high (estimated above ∼10 μm s^{-1}), there is insufficient time for the ordering kinetics to occur fully (Figure 7f) (only 43% vertical population). For low translation rates (estimated <1 μm s^{-1}) vertically oriented chains relax and preferential block surface wetting to the substrate occurs (Figure 7i,j) leading to parallel cylinders (only 7−12% vertical population). GISAXS of CZA-S-annealed films at annealing velocities of 5 and 1 μm s^{-1} (Figure 7k,l) corresponds to PS−PMMA morphology shown in Figures 7g and 7h, respectively. Ratio of first-order peak intensity (which represents perpendicular population) to the intensity of direct beam is a way to estimate the amount of perpendicular population in the film. Comparison of this ratio for Figure 7k,l reveals that the perpendicular population for the sample annealed at 5 μm s^{-1} is 3.4 times more than for the sample annealed at 1 μm s^{-1}. This again demonstrates the validity of an optimum annealing time for CZA-S annealed BCP thin films.

In addition to ∇T and sweep rate effects in CZA-S, an optimal film thickness range exists as well for vertical ordering. The air interface is able to induce progressively parallel orientation in films above 1000 nm (see Figures 2 and 3), which is in accordance to predictions via simulations by Suh et al.[51] An alternate explanation is that this can also be due to a vertical divergence of the narrow temperature profile, a consequence of heating by a hot wire at the substrate bottom. The top film surface dissipates heat to the nitrogen environment, causing this temperature gradient divergence. We believe the 1000 nm film thickness is the transition point where the CZA-S has broadened out sufficiently above the threshold sharpness (estimated between 15 and 45 °C mm^{-1}) needed for vertical orientation. This is consistent with a previous study where parallel cylinders are obtained with CZA with a temperature gradient up to 14 °C mm^{-1}.[26]

■ CONCLUSIONS

CZA of block copolymer thin films under a sharp temperature gradient $\nabla T \sim 45$ °C mm^{-1} is a facile method to control the formation of parallel or perpendicular cylinders (grain size ∼1 μm for parallel cylinders and ∼500 nm for perpendicular cylinders). Unique interdependence of microphase separation (parallel, perpendicular, and mixed morphologies) on film thickness and applied ∇T_{max} field-strength and sweep rates has been demonstrated. A sharp ∇T is essential for obtaining well-packed vertical microstructures since CZA of identical samples under a broad ∇T leads to a parallel morphology. A most promising application underpinning the CZA-S process is its ability to function in conjunction with roll-to-roll processing, a combination eminently important to thin and thick films on flexible substrates. We demonstrate the ability to generate high aspect ratio well-packed vertical nanostructures on functional flexible substrates such as Kapton and PDMS that have tremendous potential for future flexible devices ranging from UF membranes to nanoelectronics.

■ ASSOCIATED CONTENT

Ⓢ Supporting Information

Images showing the digitization process to the calculate % cylinder fraction; discussion of thickness regimes i, ii, and iv; discussion of the orientation process on flexible substrates; and a schematic image of CZA-S setup. This material is available free of charge via the Internet at http://pubs.acs.org.

■ AUTHOR INFORMATION

Corresponding Author
*E-mail: alamgir@uakron.edu.
Notes
The authors declare no competing financial interest.

■ ACKNOWLEDGMENTS

■ REFERENCES

(1) Fasolka, M. J.; Mayes, A. M. *Annu. Rev. Mater. Res.* **2001**, *31*, 323−325.

(2) Allen, N. S. In *Photochemistry and Photophysics of Polymer Materials*; Ivan, M. G., Scaiano, J. C., Eds.; John Wiley & Sons, Inc.: Hoboken, NJ, 2010; Chapter 12.

(3) Park, M.; Harrison, C.; Chaikin, P. M.; Register, R. A.; Adamson, D. H. *Science* **1997**, *276*, 1401−1404.

(4) Black, C. T.; Guarini, K. W.; Milkove, K. R.; Baker, S. M.; Russell, T. P.; Tuominen, M. T. *Appl. Phys. Lett.* **2001**, *79*, 409−411.

(5) Cheng, J. Y.; Ross, C. A.; Thomas, E. L.; Smith, H. I.; Vancso, G. J. *Appl. Phys. Lett.* **2002**, *81*, 3657−3659.

(6) Tang, C.; Lennon, E. M.; Fredrickson, G. H.; Kramer, E. J.; Hawker, C. J. *Science* **2008**, *322*, 429−432.

(7) Ji, S.; Nagpal, U.; Liao, W.; Liu, C.-C.; de Pablo, J. J.; Nealey, P. F. *Adv. Mater.* **2011**, *23*, 3692−3697.

(8) Park, S.; Lee, D. H.; Xu, J.; Kim, B.; Hong, S. W.; Jeong, U.; Xu, T.; Russell, T. P. *Science* **2009**, 1030−1033.

(9) Du, P.; Li, M.; Douki, K.; Li, X.; Garcia, C. B. W.; Jain, A.; Smilgies, D.-M.; Fetters, L. J.; Gruner, S. M.; Wiesner, U.; Ober, C. K. *Adv. Mater.* **2004**, *16*, 953−957.

(10) Crossland, E. J. W.; Kamperman, M.; Nedelcu, M.; Ducati, C.; Wiesner, U.; Smilgies, D.-M.; Toombes, G. E. S.; Hillmyer, M. A.; Ludwigs, S.; Steiner, U.; Snaith, H. J. *Nano Lett.* **2009**, *9*, 2807−2812.

(11) Zhang, Q.; Cirpan, A.; Russell, T. P.; Emrick, T. *Macromolecules* **2009**, *42*, 1079−1082.

(12) Chiu, J. J.; Kim, B. J.; Kramer, E. J.; Pine, D. J. *J. Am. Chem. Soc.* **2005**, *127*, 5036−5037.

(13) Bockstaller, M. R.; Mickiewicz, R. A.; Thomas, E. L. *Adv. Mater.* **2005**, *17*, 1331−1349.

(14) Zhao, Y.; Thorkelsson, K.; Mastroianni, A. J.; Schilling, T.; Luther, J. M.; Rancatore, B. J.; Matsunaga, K.; Jinnai, H.; Wu, Y.; Poulsen, D.; Fréchet, J. M. J.; Alivisatos, P.; Xu, T. *Nat. Mater.* **2009**, *8*, 979−985.

(15) Balazs, A. C.; Emrick, T.; Russell, T. P. *Science* **2006**, *314*, 1107−1110.

(16) Phillip, W. A.; O'Neill, B.; Rodwogin, M.; Hillmyer, M. A.; Cussler, E. L. *ACS Appl. Mater. Interfaces* **2010**, *2*, 847−853.

(17) Phillip, W. A.; Rzayev, J.; Hillmyer, M.; Cussler, E. *J. Membr. Sci.* **2006**, *286*, 144−152.

(18) Yang, S. Y.; Park, J.; Yoon, J.; Ree, M.; Jang, S. K.; Kim, J. K. *Adv. Funct. Mater.* **2008**, *18*, 1371−1377.

(19) Yang, S. Y.; Yang, J.-A.; Kim, E.-S.; Jeon, G.; Oh, E. J.; Choi, K. Y.; Hahn, S. K.; Kim, J. K. *ACS Nano* **2010**, *4*, 3817−3822.

(20) Angelescu, D. E.; Waller, J. H.; Adamson, D. H.; Deshpande, P.; Chou, S. Y.; Register, R. A.; Chaikin, P. M. *Adv. Mater.* **2004**, *16*, 1736−1740.

(21) Thurn-Albrecht, T.; DeRouchey, J.; Russell, T. P.; Kolb, R. *Macromolecules* **2002**, *35*, 8106−8110.

(22) Albert, J. N. L.; Bogart, T. D.; Lewis, R. L.; Beers, K. L.; Fasolka, M. J.; Hutchison, J. B.; Vogt, B. D.; Epps, T. H. *Nano Lett.* **2011**, *3*, 1351−1357.

(23) Mita, K.; Tanaka, H.; Saijo, K.; Takenaka, M.; Hashimoto, T. *Polymer* **2008**, *49*, 5146−5157.

(24) Mita, K.; Tanaka, H.; Saijo, K.; Takenaka, M.; Hashimoto, T. *Macromolecules* **2007**, *40*, 5923−5933.

(25) Yager, K. G.; Fredin, N. J.; Zhang, X.; Berry, B. C.; Karim, A.; Jones, R. L. *Soft Matter* **2010**, *6*, 92−99.

(26) Berry, B. C.; Bosse, A. W.; Douglas, J. F.; Jones, R. L.; Karim, A. *Nano Lett.* **2007**, *7*, 2789−2794.

(27) Bosse, A.; Douglas, J.; Berry, B.; Jones, R.; Karim, A. *Phys. Rev. Lett.* **2007**, *99*, 23−26.

(28) Singh, G.; Kulkarni, M. M.; Smilgies, D.; Sides, S.; Berry, B.; Raghavan, D.; Bucknall, D. G.; Sumpter, B.; Karim, A. *MRS Online Proc. Libr.* **2012**, DOI: 10.1557/opl.2012.443.

(29) Tang, C.; Tracz, A.; Kruk, M.; Zhang, R.; Smilgies, D.-M.; Matyjaszewski, K.; Kowalewski, T. *J. Am. Chem. Soc.* **2005**, *127*, 6918−6919.

(30) Bita, I.; Yang, J. K. W.; Jung, Y. S.; Ross, C. A.; Thomas, E. L.; Berggren, K. K. *Science* **2008**, *321*, 939−943.

(31) Kim, S. O.; Solak, H. H.; Stoykovich, M. P.; Ferrier, N. J.; De Pablo, J. J.; Nealey, P. F. *Nature* **2003**, *424*, 411−414.

(32) Mansky, P.; Liu, Y.; Huang, E.; Russell, T. P.; Hawker, C. *Science* **1997**, *275*, 1458−1460.

(33) Sivaniah, E.; Hayashi, Y.; Matsubara, S.; Kiyono, S.; Hashimoto, T.; Fukunaga, K.; Kramer, E. J.; Mates, T. *Macromolecules* **2005**, *38*, 1837−1849.

(34) Schweicher, G.; Paquay, N.; Amato, C.; Resel, R.; Koini, M.; Talvy, S.; Lemaur, V. *Cryst. Growth Des.* **2011**, *11*, 3663−3672.

(35) Liu, C.-Y.; Bard, A. J. *Appl. Phys. Lett.* **2003**, *83*, 5431−5433.

(36) Lide, D. R. *CRC Handbook of Chemistry and Physics*, 90th ed. (CD-ROM Version 2010); CRC Press: Boca Raton, FL, 2010.

(37) Lovinger, A. J.; Chua, J. O.; Gryte, C. C. *J. Phys. E: Sci. Instrum.* **1976**, *9*, 927−929.

(38) Amundson, K.; Helfand, E.; Patel, S. S.; Quan, X.; Smith, S. D. *Macromolecules* **1992**, *25*, 1935−1940.

(39) Albert, J. N. L.; Young, W.-S.; Lewis, R. L.; Bogart, T. D.; Smith, J. R.; Epps, T. H. *ACS Nano* **2012**, *6*, 459−466.

(40) Ji, S.; Liu, C.-C.; Liao, W.; Fenske, A. L.; Craig, G. S. W.; Nealey, P. F. *Macromolecules* **2011**, *44*, 4291−4300.

(41) Han, E.; Stuen, K. O.; Leolukman, M.; Liu, C.-C.; Nealey, P.; Gopalan, P. *Macromolecules* **2009**, *42*, 4896−4901.

(42) Park, S.; Lee, D. H.; Russell, T. P. *Adv. Mater.* **2010**, *22*, 1882−1884.

(43) Mark, J. E. *Polymer Data Handbook*; Oxford University Press, Inc.: New York, 1999.

(44) Beaucage, G.; Banach, M.; Vaia, R. A. *J. Polym. Sci., Part B: Polym. Phys.* **2000**, *38*, 2929−2936.

(45) Tsui, O. K. C.; Russell, T. P.; Hawker, C. J. *Macromolecules* **2001**, *34*, 5535−5539.

(46) Yager, K. G.; Berry, B. C.; Page, K.; Patton, D.; Karim, A.; Amis, E. J. *Soft Matter* **2008**, *5*, 622−628.

(47) Zhang, X.; Lacerda, S. H. D. P.; Yager, K. G.; Berry, B. C.; Douglas, J. F.; Jones, R. L.; Karim, A. *ACS Nano* **2009**, *3*, 2115−2120.

(48) Pickett, G. T.; Witten, T. A.; Nagel, S. R. *Macromolecules* **1993**, *26*, 3194−3199.

(49) Hong, S. W.; Huh, J.; Gu, X.; Lee, D. H.; Jo, W. H.; Park, S.; Xu, T.; Russell, T. P. *Proc. Natl. Acad. Sci. U. S. A.* **2012**, DOI: 10.1073/pnas.1115803109.

(50) Horvat, A.; Knoll, A.; Krausch, G.; Tsarkova, L.; Lyakhova, K. S.; Sevink, G. J. A.; Zvelindovsky, A. V.; Magerle, R. *Macromolecules* **2007**, *40*, 6930−6939.

(51) Suh, K. Y.; Kim, Y. S.; Lee, H. H. *J. Chem. Phys.* **1998**, *108*, 1253−1256.